

ELECTROWEAK RESULTS FROM THE SLD

Bruce A. Schumm*

Santa Cruz Institute for Particle Physics

University of California

Santa Cruz, CA 95064

Representing the SLD Collaboration

ABSTRACT

SLD results on electroweak asymmetries and partial widths at the Z^0 resonance peak are presented, and compared to complementary results from other facilities. The current status of Standard Model tests arising from the measurement of Z^0 boson couplings is discussed, as well as projections for future SLD data samples.

*Supported in part by DOE Contract DE-FG03-92ER40689.

1 Introduction

The first-of-its-kind SLC linear electron positron collider has proven to be a powerful facility for tests of the Standard Model via the measurement of electroweak couplings at the Z^0 pole. Its highly longitudinally-polarized electron beam ($P_e > 75\%$) and small luminous region of $(1.5 \times 0.8 \times 700) \mu\text{m}$ in (x, y, z) are particularly advantageous for the measurement of electroweak quantities. The SLD detector, described in more detail elsewhere in these proceedings,¹ is tailored to take maximum advantage of these attributes of the SLC machine.

In particular, the VXD-II CCD pixel vertex detector, in place through the 1994–5 run of the SLD, when used in combination with the SLD central drift chamber tracker (CDC), provides an uncertainty in the $r - \phi$ impact parameter of charged tracks relative to the Z^0 production point which approaches $11 \mu\text{m}$ for high-momentum tracks, and is $70 \mu\text{m}$ at $p_\perp \sqrt{\sin \theta} = 1 \text{ GeV}/c$, including the uncertainty in the location of the primary vertex. The corresponding resolution in the $r - z$ plane is $37 \mu\text{m}$ and $80 \mu\text{m}$, respectively.

For running in 1996 and beyond, the vertex detector was upgraded to the VXD-III detector,² employing improved CCD technology which allows a greater longitudinal coverage (see Fig. 1). The maximum $|\cos \theta|$ for which all tracks cross a minimum of two layers is extended by VXD-III from 0.75 to 0.90, providing a substantial increase in coverage in a region where the analyzing power of electroweak asymmetries is large. In addition, the smaller amount of material per layer, and greater radial extent of the detector, leads to a substantially improved $r - \phi$ ($r - z$) impact parameter resolution of $14 \mu\text{m}$ ($26.5 \mu\text{m}$) at high momentum and $36 \mu\text{m}$ ($42 \mu\text{m}$) at $p_\perp \sqrt{\sin \theta} = 1 \text{ GeV}/c$. Additional components of the SLD detector include a Cherenkov ring-imaging particle identification system (CRID), a gaseous central tracker (CDC), lead-liquid argon electromagnetic and hadronic calorimetry (LAC), warm-iron/Iarocci-tube hadronic calorimetry and muon identification (WIC), and a low-angle silicon-tungsten luminosity monitor.

After recording an initial sample of 10,000 Z^0 decays with low electron polarization in 1992, the SLD recorded runs of approximately 50,000 Z^0 decays in 1993, 100,000 Z^0 decays in 1994–5, and 50,000 Z^0 decays in 1996. For these latter runs, the mean electron beam polarization was $(63 \pm 1)\%$, $(77.2 \pm 0.5)\%$, and $(76.5 \pm 0.8)\%$, respectively. The 1996 mean polarization value is preliminary.

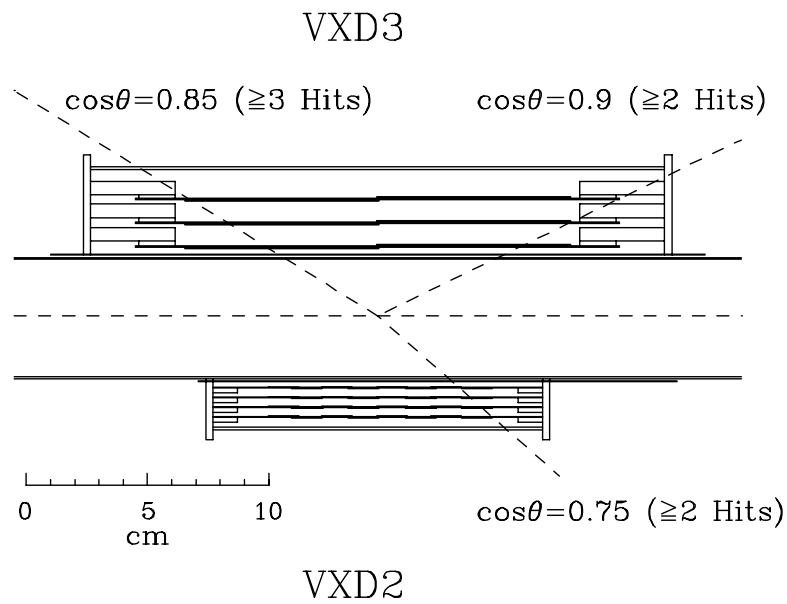
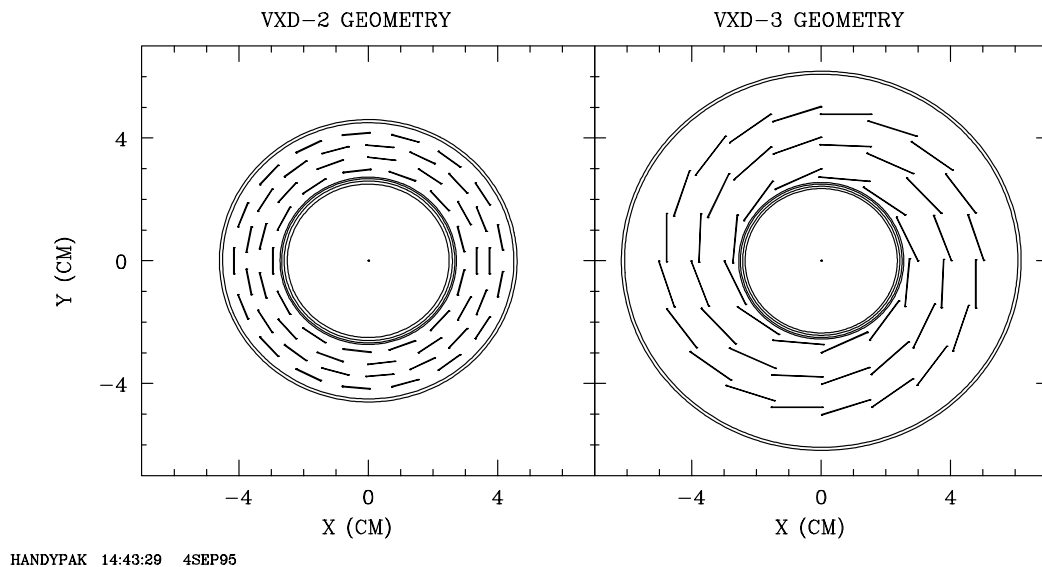


Fig. 1. Comparison between VXD-II and VXD-III geometry in (a) $r - \phi$ and (b) $r - z$.

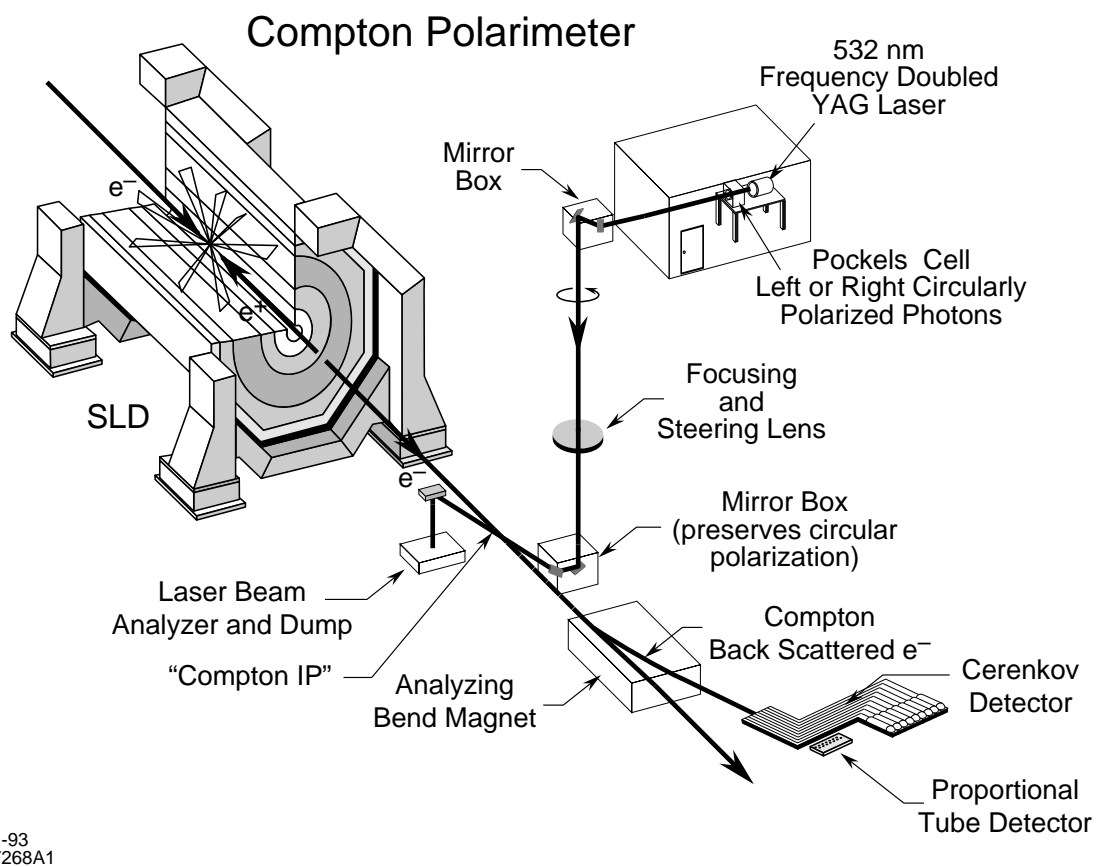


Fig. 2. Schematic diagram of the Compton Polarimeter System.

2 Electron Beam Polarimetry

Precision polarimetry of the SLC electron beam is accomplished with the Compton Polarimeter, which employs Compton scattering between the high-energy electron beam and a polarized Nd:YAG laser beam ($\lambda = 532$ nm) to probe the electron beam polarization (see Fig. 2). The Compton scattered electrons, which lose energy in the scattering process but emerge essentially undeflected, are analyzed by the first beamline dipole downstream of the SLD interaction point, beyond which they exit the beamline vacuum through a thin window, and enter a threshold Cherenkov detector segmented transverse to the beamline. The Compton cross-section polarization asymmetry

$$A(E) = \frac{\sigma_E^{J=3/2} - \sigma_E^{J=1/2}}{\sigma_E^{J=3/2} + \sigma_E^{J=1/2}} \quad (1)$$

in the differential cross section

$$\sigma_E \equiv \frac{d\sigma}{dE}(E) \quad (2)$$

between electron and laser spins aligned ($J = 3/2$) and anti-aligned ($J = 1/2$) is easily calculable within QED, and is measured at seven different values of the scattered electron energy in the Compton Cherenkov detector. The ratios between the calculated and observed asymmetry in each channel, after a small ($\sim 1\%$) correction for showering in the material upstream of the Cherenkov radiator, provide redundant measurements of the product $P_e P_\gamma$ of the electron and laser beam polarization (see Fig. 3). The laser beam polarization, typically 99.8%, is continuously monitored, allowing for the precise determination of P_e to a statistical accuracy of approximately $\delta P_e / P_e = \pm 1\%$ every three minutes. Relative systematic uncertainties in the Compton polarization measurement are summarized in Table 1. In 1993–4, a relative polarization scale uncertainty of $\pm 0.69\%$ was obtained; the preliminary 1996 value of $\pm 1.04\%$ will improve substantially once the analysis is finalized.

3 Z^0 – Fermion Couplings

At Born level, for an electron beam polarization P_e , the differential cross section for the process $e^+e^- \rightarrow Z^0 \rightarrow f\bar{f}$ is given by

$$\sigma^f(z) \propto [(v_e^2 + a_e^2 - 2a_e v_e P_e)(v_f^2 + a_f^2)](1 + z^2) + [2a_e v_e - (v_e^2 + a_e^2)P_e]4v_f a_f z, \quad (3)$$

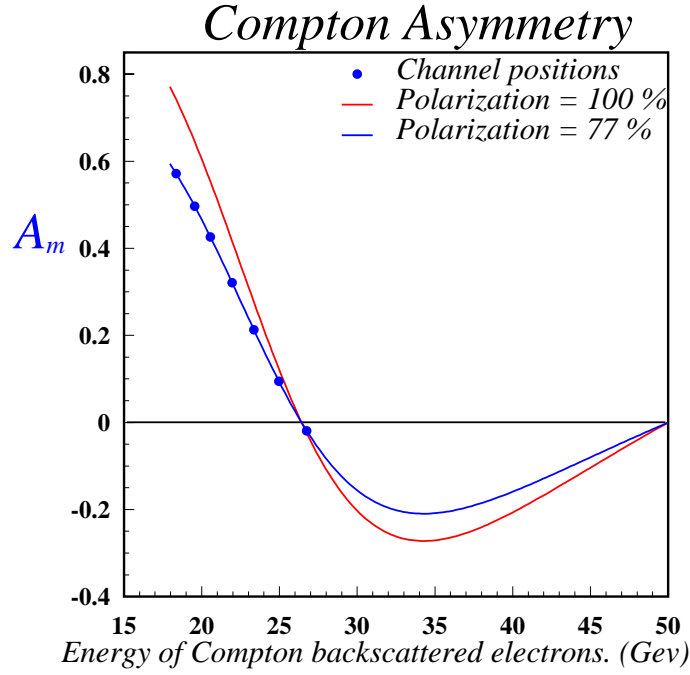


Fig. 3. Measured Compton asymmetry in the seven active channels of the threshold Cherenkov detector (dots). The upper curve is the expected energy dependence of the Compton asymmetry for the case $P_e P_\gamma = 1.0$; the scale factor relating this to the best-fit curve is thus the measured value of $P_e P_{\text{gamma}}$.

Table 1. Year-by-year systematic uncertainty on the electron beam polarization scale, as measured by the Compton Polarimeter. The 1996 result is preliminary, and is expected to be reduced after the full analysis is completed.

Uncertainty	1992	1993	1994/5	1996 (preliminary)
Laser Polarization	2.0	1.0	0.20	0.20
Detector Linearity	1.5	1.0	0.50	0.50
Detector Calibration	0.4	0.5	0.29	0.30
Electronic Noise	0.4	0.2	0.20	0.20
Interchannel Consistency	0.9	0.5	—	0.80
Sum of Polarimeter Unc.	2.7	1.6	0.67	1.03
Compton/SLD IP	—	1.1	0.17	0.18
Total P_e Uncertainty	2.7	1.9	0.69	1.04

where $z = \cos \theta$ is the angle of the final state fermion with respect to the beam axis and $\sigma^f(z) = d\sigma_f/dz$. Here, it is assumed that $P_e = +1$ for a right-handed (positive helicity) electron beam. Thus, the vector (v) and axial-vector (a) couplings are the free parameters which specify the $Z - f$ coupling. In the Standard Model,

$$v = I_3^{Weak} - 2Q \sin^2 \theta_W, \quad (4)$$

$$a = I_3^{Weak}. \quad (5)$$

With the use of a *polarized* electron beam, these coupling parameters can be extracted independently of the initial state couplings v_e and a_e , via the two following observables. The first of these, the ratio of partial widths

$$R_q \equiv \frac{\int_{-1}^1 \sigma_q(z) dz}{\sum_{q'} \int_{-1}^1 \sigma_{q'}(z) dz} = \frac{v_q^2 + a_q^2}{\sum_{q'} (v_{q'}^2 + a_{q'}^2)} = \frac{, q}{, had}, \quad (6)$$

does not require the use of polarized beams; the restriction of the denominator quark species only (no leptons) leads to the cancellation of QCD radiative effects. The second of these, the polarized forward-backward asymmetry, does require the use of polarized beams:

$$\tilde{A}_{FB}^f(z) = \frac{[\sigma_L^f(z) - \sigma_L^f(-z)] - [\sigma_R^f(z) - \sigma_R^f(-z)]}{\sigma_L^f(z) + \sigma_L^f(-z) + \sigma_R^f(z) + \sigma_R^f(-z)} = |P_e| A_f \frac{2z}{1 + z^2}, \quad (7)$$

where the subscript L (R) refers to left-handed (right-handed) electron beams, and

$$A_f \equiv \frac{2v_f a_f}{v_f^2 + a_f^2} \quad (8)$$

is the quantitative extent of parity violation in the $Z^0 - f$ coupling. These two measurements specify the $Z^0 - f$ coupling in generality.

Finally, one can define the left-right asymmetry

$$A_{LR} = \frac{1}{P_e} \frac{\sum_{f \neq e} \int_{-1}^1 \sigma_L^f(z) dz - \sum_{f \neq e} \int_{-1}^1 \sigma_R^f(z) dz}{\sum_{f \neq e} \int_{-1}^1 \sigma_L^f(z) dz + \sum_{f \neq e} \int_{-1}^1 \sigma_R^f(z) dz} = \frac{1}{P_e} [P_e \frac{2v_e a_e}{v_e^2 + a_e^2}] = A_e, \quad (9)$$

where the sum is restricted to all final states except e^+e^- in order to avoid having to unravel t-channel effects. This is a particularly potent way to measure $\sin^2 \theta_W$ provided P_e can be measured precisely:

$$A_{LR} = \frac{2(1 - 4 \sin^2 \theta_W)}{1 + (1 - 4 \sin^2 \theta_W)^2}. \quad (10)$$

This makes A_{LR} very sensitive to the weak mixing angle:

$$\frac{dA_{LR}}{d\sin^2\theta_W} \simeq -7.8. \quad (11)$$

It should be pointed out that these relations have been derived for the case of the Born-level interaction. However, since the Z^0 -pole measurements now provide the most accurate constraints on Standard Model consistency, the convention that has arisen is to incorporate higher order effects by making Eq. (10) the *definition* of the weak mixing angle. This is denoted by the notation $\sin^2\theta_W^{eff}$; higher order effects must then be explicitly accounted for when comparing this value with that of non- Z^0 -pole measurements.

4 Measurement of A_{LR}

In practice, A_{LR} is measured with hadronic final states only, with the leptonic final states considered separately (see below). In 1996, a 99.9% pure hadronic sample was selected by requiring that the absolute value of the energy imbalance (ratio of vector to scalar energy sum in the calorimeter) be less than 0.6, that there be at least 22 GeV of visible calorimetric energy, and at least four charged tracks reconstructed in the central tracker. This selection was 92% efficient, resulting in a sample of 28,713 (22,662) hadronic Z^0 decays recorded with left-handed (right-handed) electron beams. Including a +0.06% experimental correction for false asymmetries and backgrounds, this yields a value

$$A_{LR}^{meas} = \frac{1}{P_e} \frac{N_L - N_R}{N_L + N_R} = 0.1541 \pm 0.0057 \pm 0.0016, \quad (12)$$

where the systematic uncertainty is dominated by the uncertainty in the polarization scale. To correct this to a Z^0 -pole asymmetry, the value must be raised by 1.9% to account for the effects of $Z - \gamma$ interference, yielding the 1996-only preliminary result

$$A_{LR}^0 = 0.1570 \pm 0.0057 \pm 0.0017, \quad (13)$$

$$\sin^2\theta_W^{eff} = 0.23025 \pm 0.00073 \pm 0.00021. \quad (14)$$

5 Leptonic Final State Asymmetries

Parity violation in the Z^0 -lepton couplings is measured by fits to the differential cross section (3) separately for the three leptonic final states, including the effects

Table 2. Lepton sample statistics.

Channel	Sample Size	Efficiency ($ \cos\theta < 0.7$)	Purity	Dominant Background
e^+e^-	4527	92%	99.3%	$\tau^+\tau^-$
$\mu^+\mu^-$	3788	96%	$> 99.9\%$	—
$\tau^+\tau^-$	3748	90%	97.0%	$e^+e^-, \gamma\gamma$

of t-channel exchange for the $Z^0 \rightarrow e^+e^-$ final state. Leptonic final states in the range $|\cos\theta| < 0.7$ are selected by requiring that events have between two and eight charged tracks in the CDC, at least one track with $p \geq 1$ GeV/c, and a net charge of +1(−1) in the positive (negative) lepton hemisphere. Events are identified as Bhabha candidates if the total calorimetric energy associated with the two most energetic tracks is greater than 45 GeV. On the other hand, if there is less than 10 GeV of associated energy for each track, and there is a two-track combination with an invariant mass of greater than 70 GeV/ c^2 , the event is classified as a muon candidate. Finally, events are classified as tau candidates provided the $\tau^+\tau^-$ invariant mass is less than 70 GeV/ c^2 , with a separation angle of at least 160° , and a mass of less than 1.8 GeV/ c^2 and associated energy of less than 27.5 GeV for each of the two tau candidates in the event. The resulting efficiencies and purities are shown in Table 2.

An example of the resulting polar angle distribution (in this case for muons from the 1993 and 1994–5 analyses) is shown in Fig. 4. The results of fits to the angular distributions, after correcting for the small background contamination, are summarized in Table 3. For the electron final state, t-channel effects are incorporated into the angular distribution, while for the tau final state, a small $\cos\theta$ -dependent efficiency correction has been applied to account for the effects of the correlation between visible energy and net tau polarization (the “V-A effect”) on the tau identification efficiency. Note that all channels provide information about A_e , which comes in through the left-right cross section asymmetry. The final-state lepton couplings are constrained by the angular distributions; for muons, the SLD value $A_\mu^{SLD} = 0.102 \pm 0.034$ is competitive with the overall LEP value $A_\mu^{LEP} = 0.155 \pm 0.016$ (Ref. 3). A combination of the values in Table 3,

SLD $\mu^+\mu^-$ angular distribution

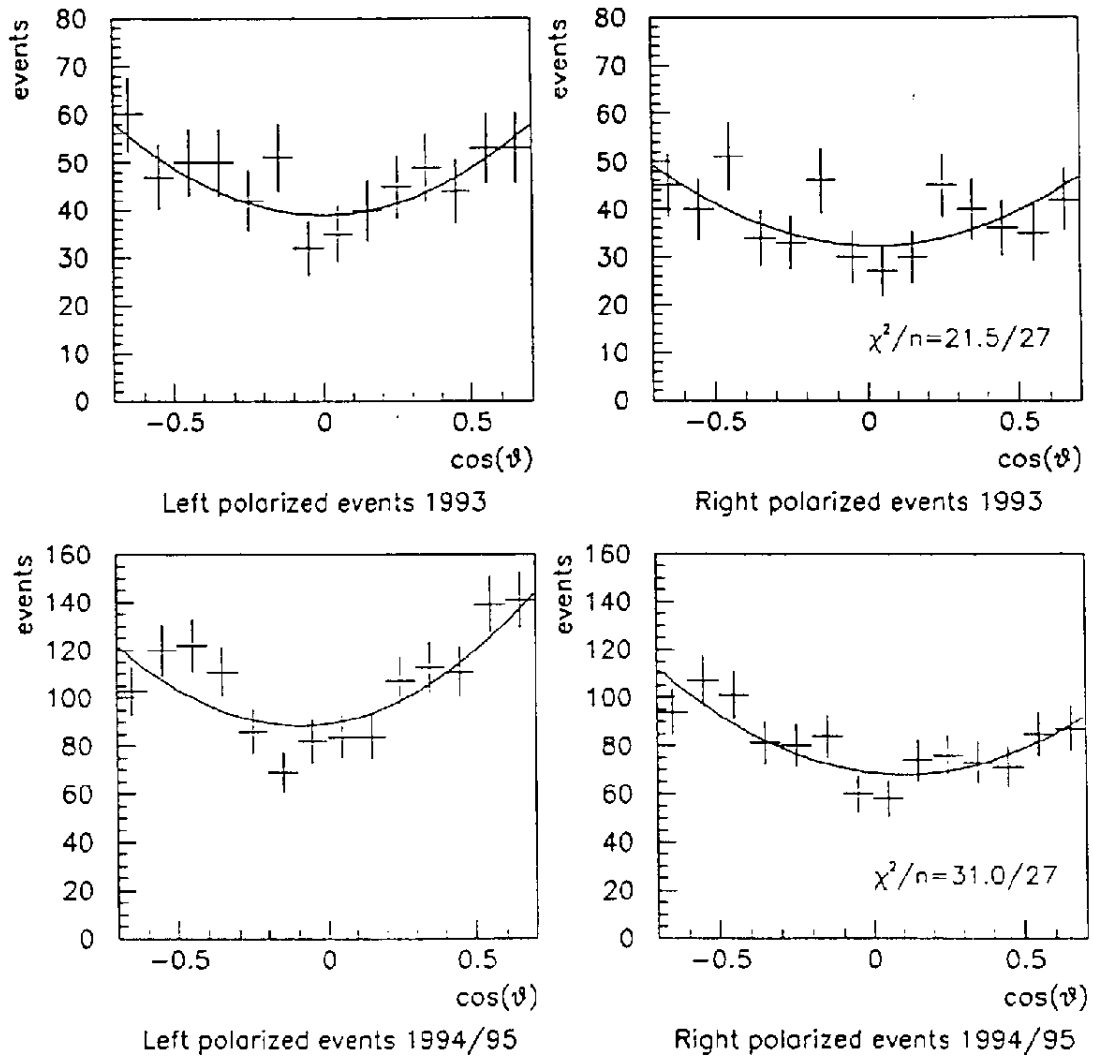


Fig. 4. Angular distributions for SLD μ -pairs, separately for left- and right-handed electron beams.

Table 3. Results of the lepton asymmetry analysis.

Channel	Sample	A_e	A_μ	A_τ
e^+e^-	4527	$0.156 \pm 0.019 \pm 0.001$	$0.102 \pm 0.034 \pm 0.001$	$0.195 \pm 0.034 \pm 0.003$
$\mu^+\mu^-$	3788	$0.169 \pm 0.022 \pm 0.001$		
$\tau^+\tau^-$	3748	$0.128 \pm 0.022 \pm 0.002$		

assuming lepton universality, yields the value

$$\sin^2 \theta_W^{eff} = 0.2310 \pm 0.0014. \quad (15)$$

6 SLD Combined Value of $\sin^2 \theta_W^{eff}$

Combining the 1996 A_{LR} and lepton channel measurements with the 1993–5 A_{LR} result⁴ yields the SLD combined value

$$\sin^2 \theta_W^{eff} = 0.23055 \pm 0.00041, \quad (16)$$

which is 2.8σ lower than the preliminary LEP combined value $\sin^2 \theta_W^{eff} = 0.23196 \pm 0.00028$ (Ref. 3). This discrepancy is reflected in Fig. 5, which exhibits the constraints on Z^0 propagator vacuum polarization effects provided by precise electroweak data. The two axis parameters, “S” and “T,” represent the size of generic weak-isospin conserving and weak-isospin violating vacuum polarization effects, respectively,⁵ with the point (0,0) corresponding to the Standard Model expectation with $m_t = 175 \text{ GeV}/c^2$ and $m_H = 300 \text{ GeV}/c^2$. The probability that the four measurement trajectories are consistent with a single point in (S,T) space is about 5%. If this poor goodness-of-fit is not statistical, conclusions regarding overall Standard Model consistency depend greatly on which of the two Z^0 -pole asymmetry measurements is correct. If the SLD measurement is wrong, then the remaining measurements are consistent with the Standard Model contour, and suggest an intermediate Higgs boson mass. If instead the LEP measurement is in error, then the entire Standard Model contour lies outside the best-fit region, with the best consistency occurring for a light Higgs mass.

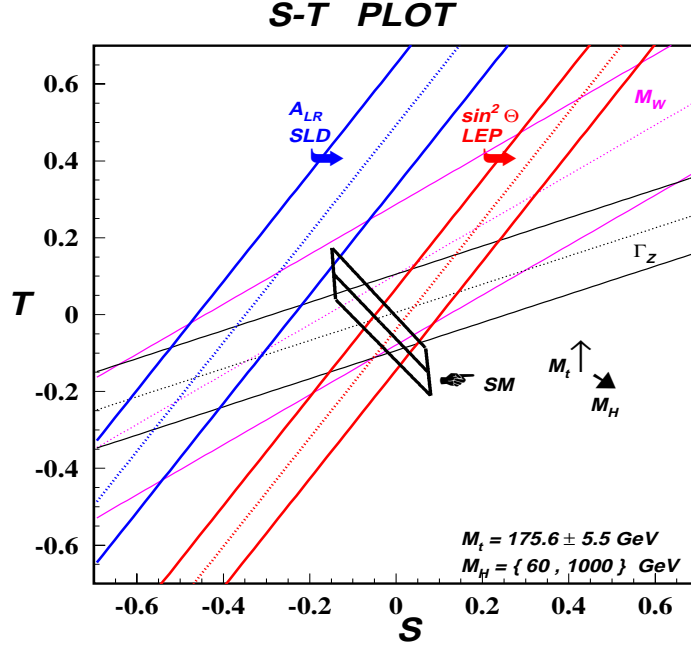


Fig. 5. Plot of observed trajectories for Z^0 vacuum polarization corrections, for generic weak-isospin conserving (S) and violating (T) corrections.

7 Heavy Quark Identification—The Mass Tag

The SLD mass tag is described in more detail elsewhere in these proceedings.¹ Secondary vertices from decays of hadrons containing heavy (b , c) quarks are observed as points displaced from the SLD interaction point which have a high probability that two or more tracks overlap. The mass tag is then applied to the “ p_{\perp} -corrected” secondary vertex mass

$$M = \sqrt{M_{raw}^2 + p_{\perp}^2} + p_{\perp} \quad (17)$$

of tracks in the secondary vertex, where p_{\perp} is the transverse component of the secondary vertex momentum resultant with respect to the secondary vertex flight direction. Two samples—bottom and charm—are identified within the regions $M > 2.0$ and $0.6 < M < 2.0$, respectively, where M is measured in GeV/c^2 . The M distribution for the 1996 data is shown in Fig. 6, compared to its MC expectation, which is broken up into its bottom, charm, and light (uds) contributions.

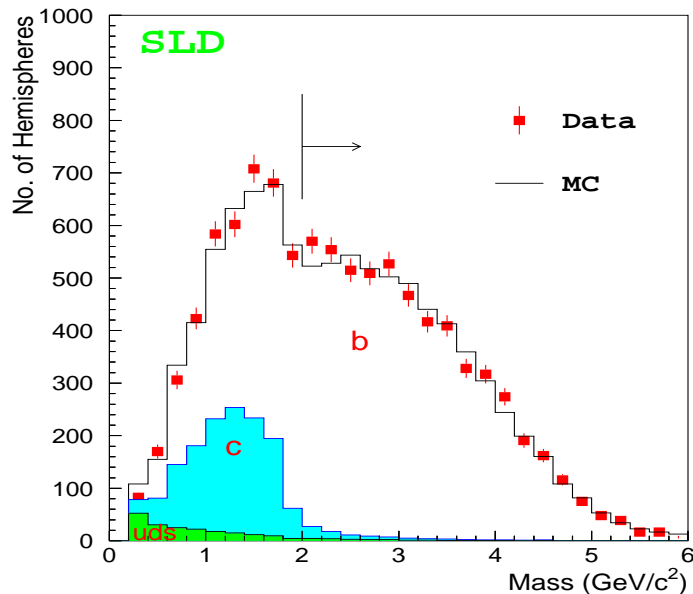


Fig. 6. Distribution in the p_{\perp} -corrected mass M for the 1996 data. The region $0.6 < M < 2.0$ is the charm-enhanced region, while $M > 2.0$ is the bottom-enhanced region.

8 Measurement of Partial-Width Ratios

The SLD measures the partial-width ratios R_b and R_c of bottom quark and charm quark production relative to all hadronic production.

8.1 Measurement of R_b

In the bottom quark region ($M > 2.0 \text{ GeV}/c^2$), the 1993–5 hemisphere b-tagging efficiency, estimated from Monte Carlo, was 35.6%, with a sample purity of 98.0%. In 1996, with VXD-III, a hemisphere tagging efficiency of 47.9% was achieved with essentially the same sample purity. With a hemisphere tag, both the single-tag and double-tag rates are observable, leading to the ability to constrain an additional parameter in the R_b measurement. Thus, allowing the hemisphere tagging efficiency to be constrained simultaneously with R_b greatly reduces systematic error by removing much of the dependence upon Monte Carlo modeling.⁶ The resulting value of R_b for the 1993–5 data is

$$R_b = 0.2142 \pm 0.0034 \pm 0.0016, \quad (18)$$

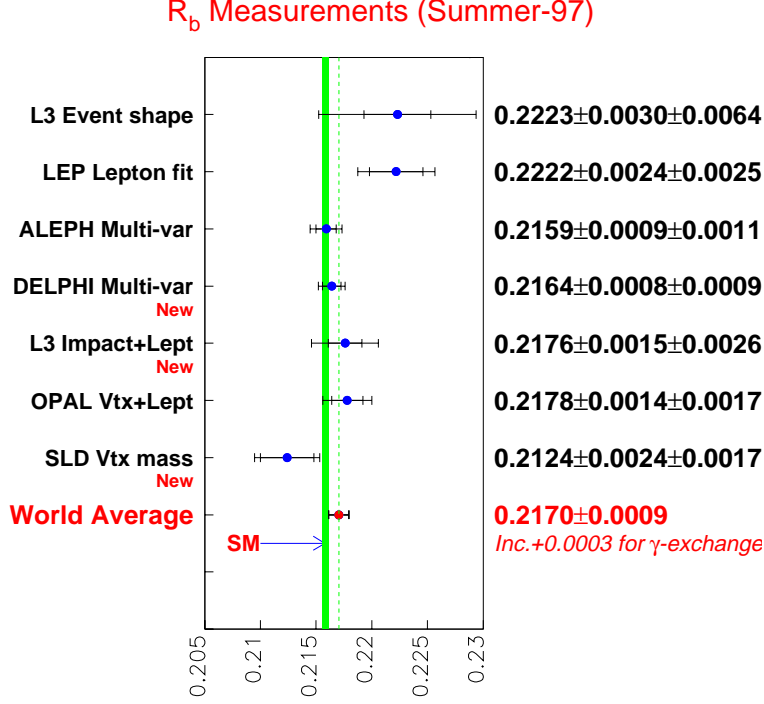


Fig. 7. Compendium of results for the measurement of R_b .

while the 1996 preliminary number is

$$R_b = 0.2102 \pm 0.0034 \pm 0.0022, \quad (19)$$

leading to an SLD combined preliminary value

$$R_b = 0.2124 \pm 0.0024 \pm 0.0017, \quad (20)$$

with the dominant systematic uncertainty arising from unmodeled smearing of the SLD tracking system. As a check, the hemisphere tagging efficiency extracted from the data was $(35.1 \pm 0.6)\%$ for 1993–5, and $(47.9 \pm 0.8)\%$ for 1996, in good agreement with Monte Carlo expectations. A comparison of the SLD R_b result with LEP results is shown in Fig. 7.

8.2 Measurement of R_c

As seen in Fig. 6, the restriction to the region $0.6 < M < 2.0$ provides a charm sample with a purity of less than 50%. To increase the charm sample purity, an additional cut requiring $(15M - P_{vtx}/c) < 10 \text{ GeV}/c^2$ is applied, where P_{vtx} is the magnitude of the secondary vertex momentum resultant. This cut takes

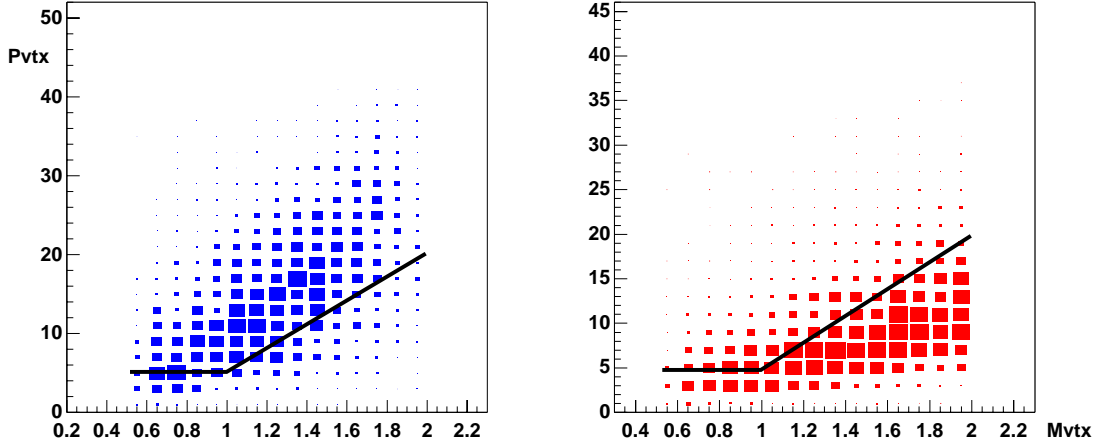


Fig. 8. Plot of the Monte Carlo distribution of P_{vtx} vs M (the p_{\perp} -corrected mass) separately for bottom and charm decays in the charm sample region $0.6 < M < 2.0$.

advantage of the fact that a secondary vertex with low mass which is really due to an underlying charm event should reflect the hard charm-quark fragmentation (see Fig. 8). The resulting MC expectation for the hemisphere charm quark tagging efficiency for 1993–5 (1996) is 10.6% (14.8%), with a purity in both cases of about 67%.

With a relatively low purity, simultaneously constraining the charm-tagging efficiency alone is not enough to sufficiently reduce systematic uncertainty. Thus, a third constraint from data, the mixed bottom and charm tagged fraction (charm tag in one hemisphere, bottom tag in the other) allows the additional extraction of the bottom-tagging efficiency of the charm selection, tightly constraining the charm sample purity. The resulting 1993–6 combined preliminary measurement

$$R_c = 0.181 \pm 0.012 \pm 0.008 \quad (21)$$

is then statistics-dominated, with a systematic uncertainty dominated by uncertainty in the SLD IP position. The SLD combined result is compared to LEP measurements in Fig. 9.

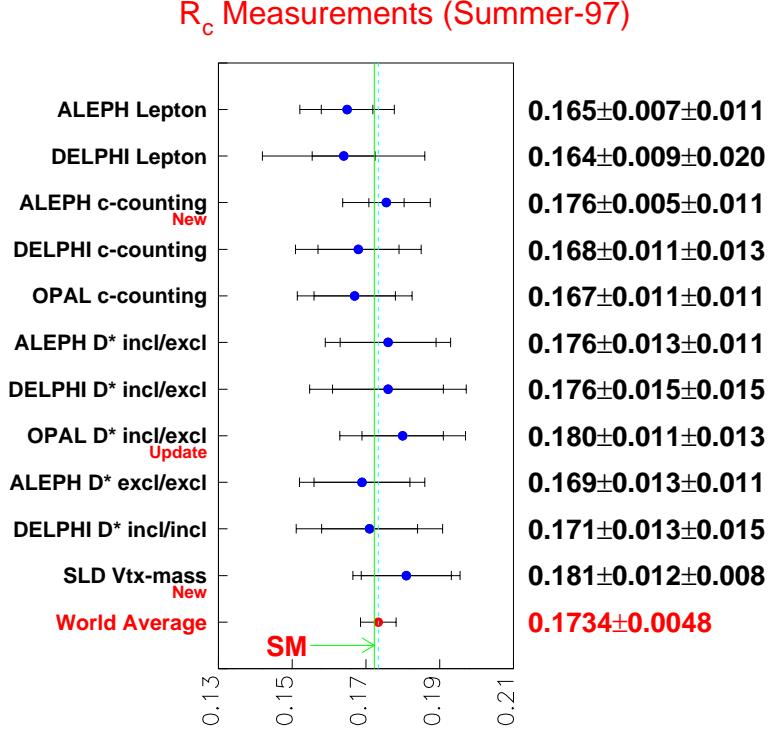


Fig. 9. Compendium of results for the measurement of R_c .

9 Heavy Quark Polarized Forward-Backward Asymmetries

A technical issue of some importance in the measurement of quark forward-backward asymmetries is that of QCD radiative effects, which nominally reduce Z^0 pole asymmetries by 3–4%, with some dependence upon final state quark mass.⁷ However, the analysis procedure, due to the effects of heavy-quark tagging, and estimation of the underlying quark charge and direction, tends to bias against multijet events, thus reducing the effects of QCD radiation. After taking into account analysis effects, the typical remaining QCD correction is 1–1.5%. This issue has been studied individually for each of the five approaches discussed here, and has been incorporated in the numbers quoted for each analysis.

9.1 Cascade Kaon Analysis

In this analysis, the SLD CRID is used to identify charged kaons from the $b \rightarrow c \rightarrow s$ cascade. The identified kaon thus provides an estimate of the charge of the

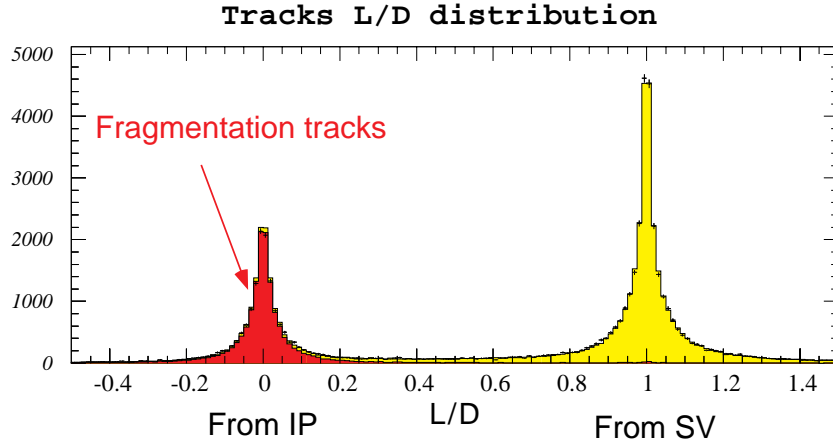


Fig. 10. Plot of the L/D distribution of CRID-tagged kaons (crosses). The corresponding MC expectation (histogram) is divided between fragmentation and secondary vertex tracks, showing the separation achieved by the vertexing system.

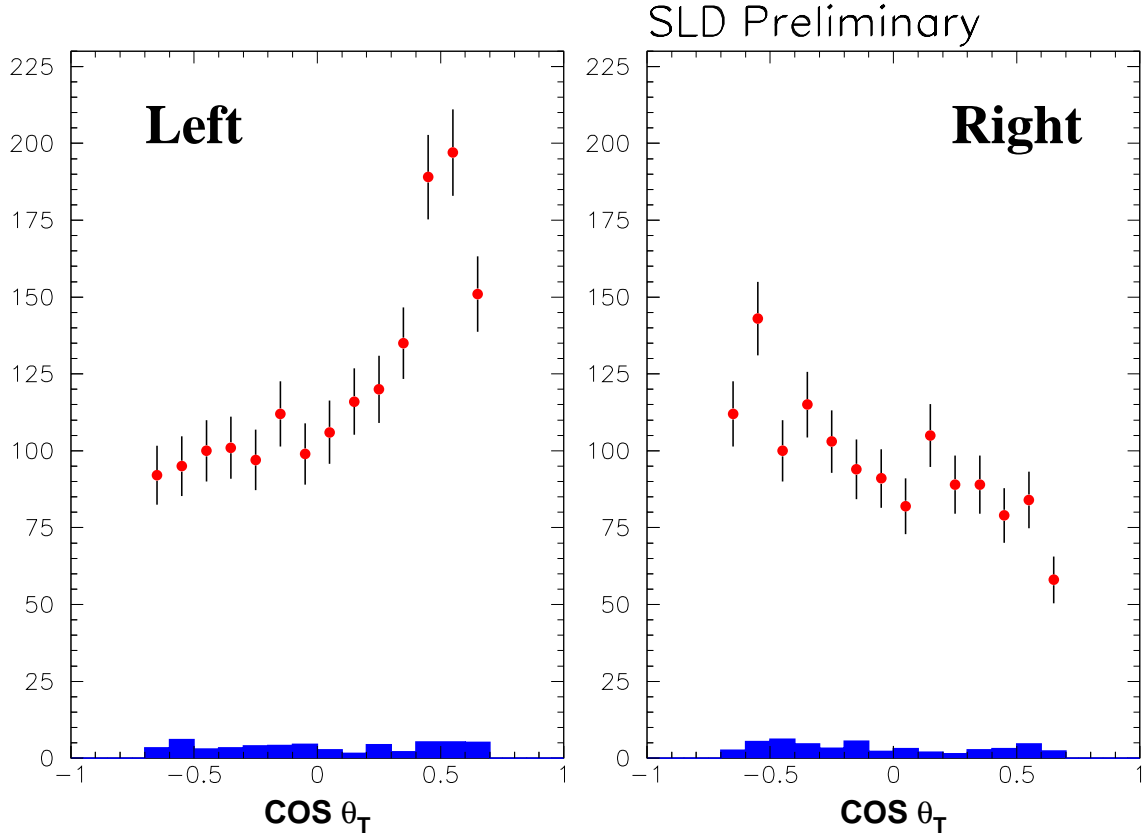


Fig. 11. Angular distribution of $B \rightarrow K^-$ candidates, separately for left- and right-handed electron beams.

underlying b quark, while the flight direction is estimated with the thrust axis. Only kaons from events identified as $Z \rightarrow b\bar{b}$ candidates by the standard mass tag are considered. In addition, rejection of fragmentation kaons is achieved by requiring the quantity L/D to be greater than 0.5, where D is the secondary vertex flight distance, and L the distance along this flight direction from the primary vertex to the point of closest approach of the kaon candidate (see Fig. 10). The resulting angular distribution of the signed thrust axis, separately for left- and right-handed electron beams, is shown in Fig. 11. A fit to the distribution yields the preliminary value

$$A_b = 0.891 \pm 0.083 \pm 0.113, \quad (22)$$

where the dominant systematic error is due to the uncertainty in the wrong-sign fraction $F(B^\pm \rightarrow K^\mp)$; an analysis of existing ARGUS data is underway to improve the empirical constraint on this quantity.

9.2 Momentum-Weighted Track Charge Analysis

In this analysis, $Z^0 \rightarrow b\bar{b}$ events are again identified with the standard mass tag, but the charge of the underlying b quark is determined via a momentum-weighted track charge sum

$$Q = - \sum_{tracks} q_i |\vec{p}_i \cdot \hat{T}|^{0.5} \text{sgn}(\vec{p}_i \cdot \hat{T}), \quad (23)$$

where \hat{T} is the thrust axis, and the sum runs over all tracks in the event. Positive Q indicates that a b quark lies along the thrust axis, while negative Q indicates that a \bar{b} quark lies along the thrust axis. It is possible to measure the correct-signing probability of the track charge sum by comparing the distribution of the data in $|Q|$ to that of the variable

$$Q' = - \sum_{tracks} q_i |\vec{p}_i \cdot \hat{T}|^{0.5}. \quad (24)$$

The distribution in Q' is proportional to the combination of the intrinsic width and separation between the b and \bar{b} distributions, while the width of the full event $|Q|$ distribution is solely proportional to the intrinsic width of the hemispheric Q distribution. Formally, since the hemispheric Q distribution is nearly Gaussian, the correct signing probability can be written

$$P_{corr}(|Q|) = \frac{1}{1 + \exp(-\alpha|Q|)}, \quad (25)$$

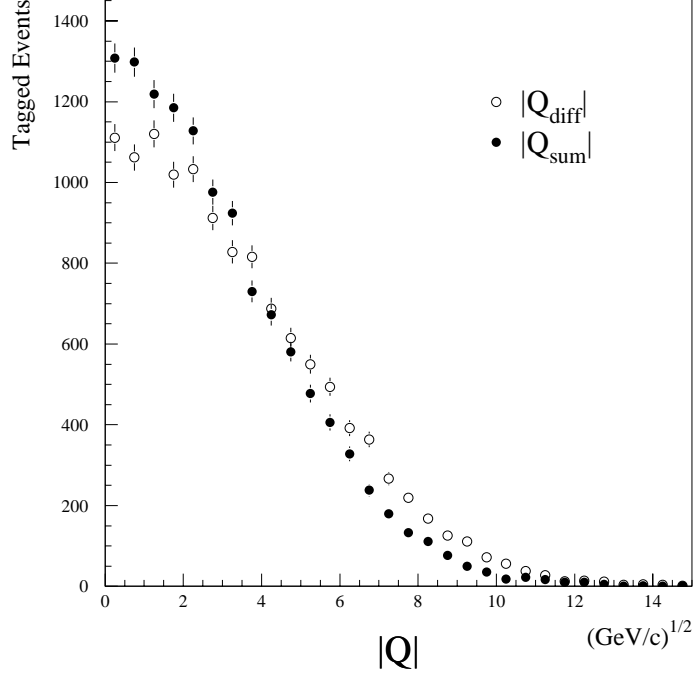


Fig. 12. Overlay plot of the Q and Q' distributions for the 1994–5 data. The difference in the widths of the two distributions is related to the analyzing power of the track-charge sum.

where

$$\alpha = \frac{2\sqrt{\langle |Q|^2 \rangle - \sigma_{Q'}^2}}{\sigma_{Q'}^2}. \quad (26)$$

Figure 12 shows the $|Q|$ (dots) and Q' (circles) distributions for the $Z \rightarrow b\bar{b}$ sample; the amount of observed extra width in the Q' distribution corresponds to a mean correct-signing probability of 68%. Use of this self-calibration technique allows Monte Carlo modeling uncertainties to be largely avoided. The resulting fit to the b -quark angular distributions yields the preliminary value

$$A_b = 0.911 \pm 0.045 \pm 0.045, \quad (27)$$

where the dominant contribution to the systematic uncertainty is from the statistics of the track-charge self-calibration.

9.3 Inclusive Semileptonic Decay Analysis

Leptons from the semileptonic processes $b \rightarrow cl^-\bar{\nu}_l$ and $c \rightarrow sl^+\nu_l$ simultaneously provide information about the underlying quark charge as well as the quark direction. The lepton total momentum and transverse momentum with respect to the jet axis, as well as the hemisphere secondary vertex mass if available, provide information which permits the statistical separation between leptons from the decay of primary bottom and charm quarks. In hadronic events, muons are identified via CRID identification and their penetration through the Warm Iron Calorimeter, while electrons are identified with a neural net incorporating CRID identification, shower shape, and the momentum/energy match between the CDC and Liquid Argon Calorimeter. The resulting angular distributions are fit simultaneously for A_b and A_c . Correcting for backgrounds and the effects of $B - \bar{B}$ mixing yields the preliminary results

$$A_b = 0.877 \pm 0.068 \pm 0.047, \quad (28)$$

$$A_c = 0.614 \pm 0.104 \pm 0.074. \quad (29)$$

9.4 Inclusive Charm Analysis

The inclusive charm A_c measurement makes use of the same charm sample as the corresponding R_c analysis. The sign of the underlying charm quark is determined from the net charge of the secondary vertex if not zero (51% of the time), or from the charge of an identified kaon if available (33% of the time). The fit to the resulting angular distributions yields the preliminary value

$$A_c = 0.662 \pm 0.068 \pm 0.042. \quad (30)$$

9.5 Exclusive Charm Analysis

The SLD reconstructs exclusive charm signals in four modes: $D^{*+} \rightarrow D^0\pi^+$, with $D^0 \rightarrow K^-\pi^+$, $K^-\pi^+\pi^0$, $K^-\pi^+\pi^+\pi^-$, and $D^+ \rightarrow K^-\pi^+\pi^+$. Figure 13 shows the difference between the $K-\pi$ and $D^0-\pi$ invariant mass for $D^* \rightarrow D^0\pi$ ($D^0 \rightarrow K\pi$) candidates. A clear peak with low background is observed. Although the overall charm reconstruction efficiency is low (4%), the exclusive signals reveal the sign and flight direction of the underlying charm quark with high accuracy. A fit to

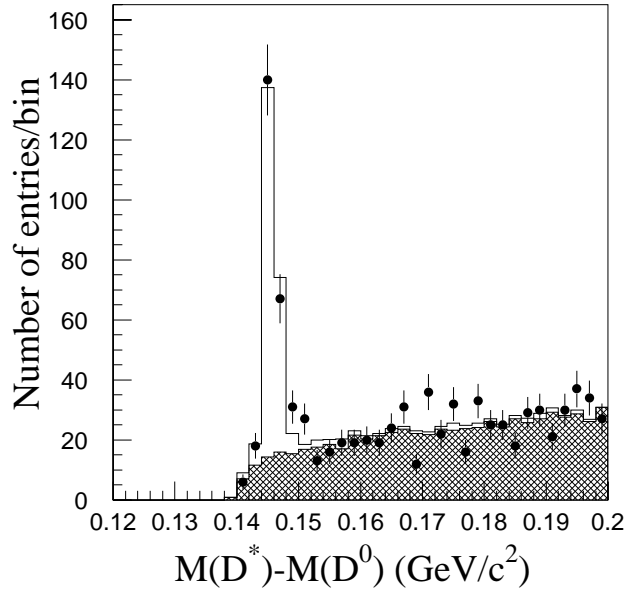


Fig. 13. Plot of the mass difference distribution for the decay chain $D^{+*} \rightarrow D^0 \pi^+$, $D^0 \rightarrow K^- \pi^+$. A clear charm signal is observed.

the resulting angular distributions yields the preliminary result

$$A_c = 0.64 \pm 0.11 \pm 0.06. \quad (31)$$

9.6 Summary of SLD Hadronic Final State Asymmetry Measurements

A synopsis of the SLD heavy quark polarized forward-backward asymmetry results is presented in Table 4. A weighted average of the individual results, incorporating the effects of experimental correlations, yields the 1993–5 preliminary SLD averages

$$A_b = 0.898 \pm 0.052, \quad (32)$$

$$A_c = 0.647 \pm 0.060, \quad (33)$$

to be compared with the Standard Model expectations $A_b = 0.935$ and $A_c = 0.667$. Comparisons with results from LEP are shown in Figs. 14 and 15; for the LEP measurements, the value of the heavy quark coupling parameter A_q has been obtained from the *unpolarized* forward-backward asymmetry $A_{FB}^q = \frac{3}{4} A_e A_q$, assuming the LEP/SLD weighted average A_l for A_e .

Table 4. Results of the b and c quark asymmetry analyses.

Approach	A_b	A_c
Jet Charge Sum	$0.911 \pm 0.045 \pm 0.045$	—
Inclusive Leptons	$0.877 \pm 0.068 \pm 0.047$	$0.614 \pm 0.104 \pm 0.074$
Cascade Kaon	$0.891 \pm 0.083 \pm 0.113$	—
Exclusive Charm	—	$0.64 \pm 0.11 \pm 0.06$
Inclusive Charm	—	$0.662 \pm 0.068 \pm 0.042$
SLD Average	0.898 ± 0.052	0.647 ± 0.060

A_b Measurements (Summer-97)

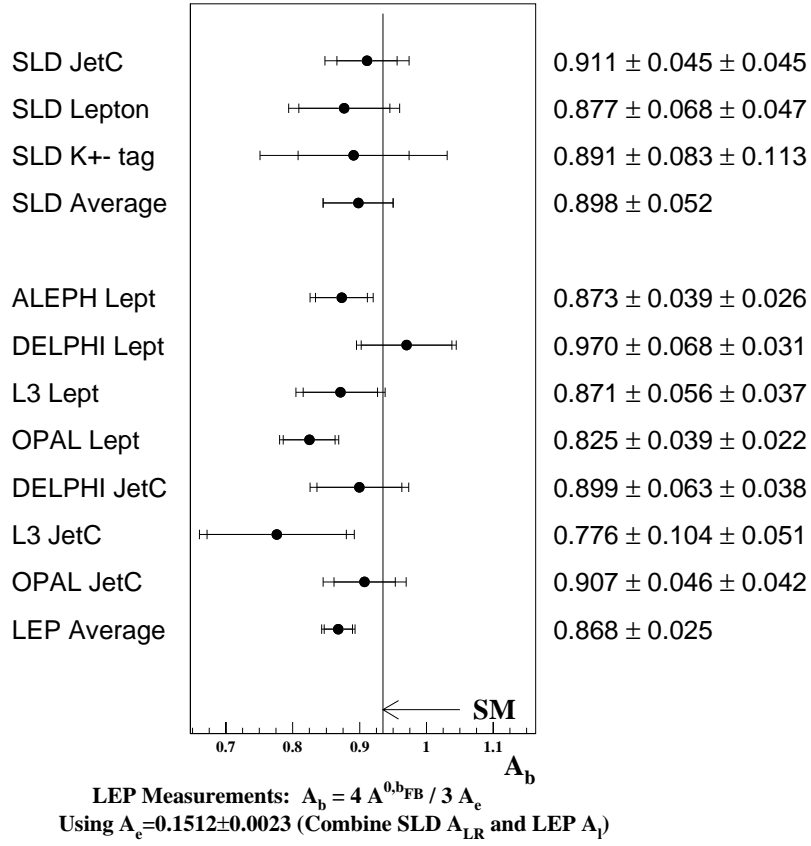
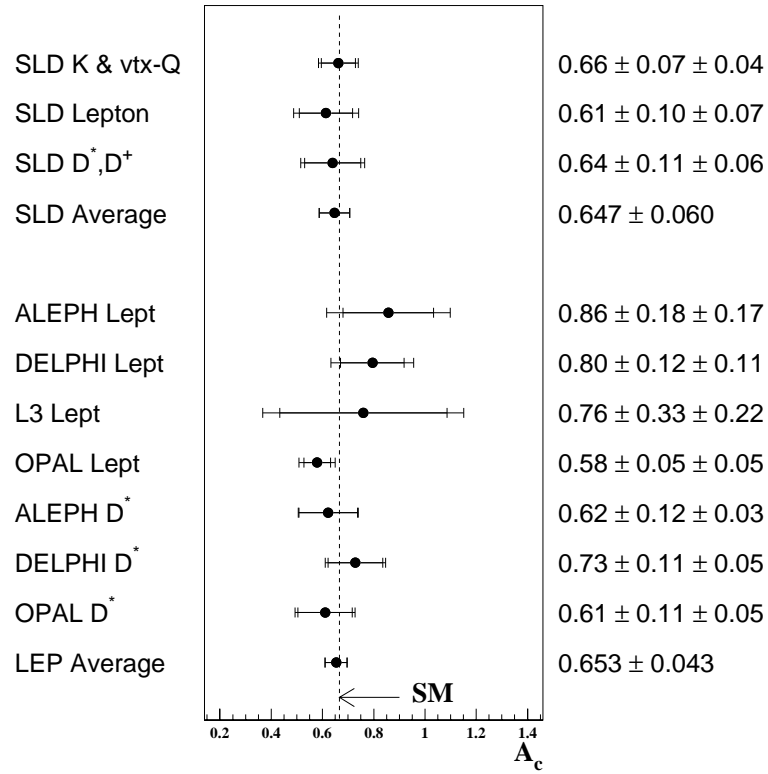


Fig. 14. Compendium of results for the measurement of A_b .

A_c Measurements (Summer-97)



LEP Measurements: $A_c = 4 A^{0_{cFB}} / 3 A_e$
 Using $A_e = 0.1512 \pm 0.0023$ (Combine SLD A_{LR} and LEP A_l)

Fig. 15. Compendium of results for the measurement of A_c .

10 Global Fits for $Z - b$ Coupling Parameters

In addition to R_b and \tilde{A}_{FB}^b , there are a number of other observables sensitive to $Z - b$ coupling parameters. Observables sensitive to the overall coupling strength are R_b , $R_z = \sigma_{had}/\sigma_{l+l-}$, the peak hadronic cross section σ_{had}^0 , and R_c . Observables sensitive to the extent of parity violation in the $Z - b$ coupling are the polarized and unpolarized forward-backward asymmetries \tilde{A}_{FB}^b and A_{FB}^b . However, a number of these depend strongly on $\sin^2 \theta_W^{eff}$, so in order to incorporate all of these observables into a constraint on $Z - b$ couplings, it is necessary to do a simultaneous fit for R_b , A_b , and $\sin^2 \theta_W^{eff}$, where the value of $\sin^2 \theta_W^{eff}$ used in the fit is that measured from leptonic final states only. The procedure for doing this fit has been developed in Ref. 8. The result of this fit, projected into the $\sin^2 \theta_W^{eff} - R_b$ plane, is shown in Fig. 16, while the projection of the fit into the $\sin^2 \theta_W^{eff} - A_b$ plane is shown in Fig. 17. The results are expressed in terms of the variables δs , δr , and δa , which are the differences between observation and the Standard Model expectation for $\sin^2 \theta_W^{eff}$, roughly $-1/4 R_b$ and $-3/5 A_b$, respectively. The Standard Model expectation has been calculated for the values $m_t = 180 \text{ GeV}/c^2$, $m_H = 300 \text{ GeV}/c^2$, $\alpha_S(M_Z^2) = 0.117$, and $\alpha_{EM}(M_Z^2) = (128.96)^{-1}$, corresponding to the point (0,0) on each plot. The Standard Model contour shown corresponds to the range $100 < m_H < 1000$ and $170 < m_t < 190$. In the $\sin^2 \theta_W^{eff} - R_b$ plane, the fit is within one standard deviation of the Standard Model contour, reflecting the improved consistency of current R_b measurements with the Standard Model. A preference for low Higgs mass, coming from the weak mixing angle measurement, has the same empirical source as that observed in Fig. 5. In the $\sin^2 \theta_W^{eff} - A_b$ plane, however, agreement is not observed between experiments and the Standard Model expectation, primarily due to the combination of the low forward-backward asymmetry measurement from LEP with the low weak mixing angle measurement from the SLD. However, the SLD polarized asymmetry measurement, which is independent of $\sin^2 \theta_W^{eff}$, is in agreement with the Standard Model expectation, but does not have enough statistical power to nullify the effect of the LEP measurement. Clearly, a more accurate measurement of \tilde{A}_{FB}^b from the SLD is crucial if this issue is to be resolved.

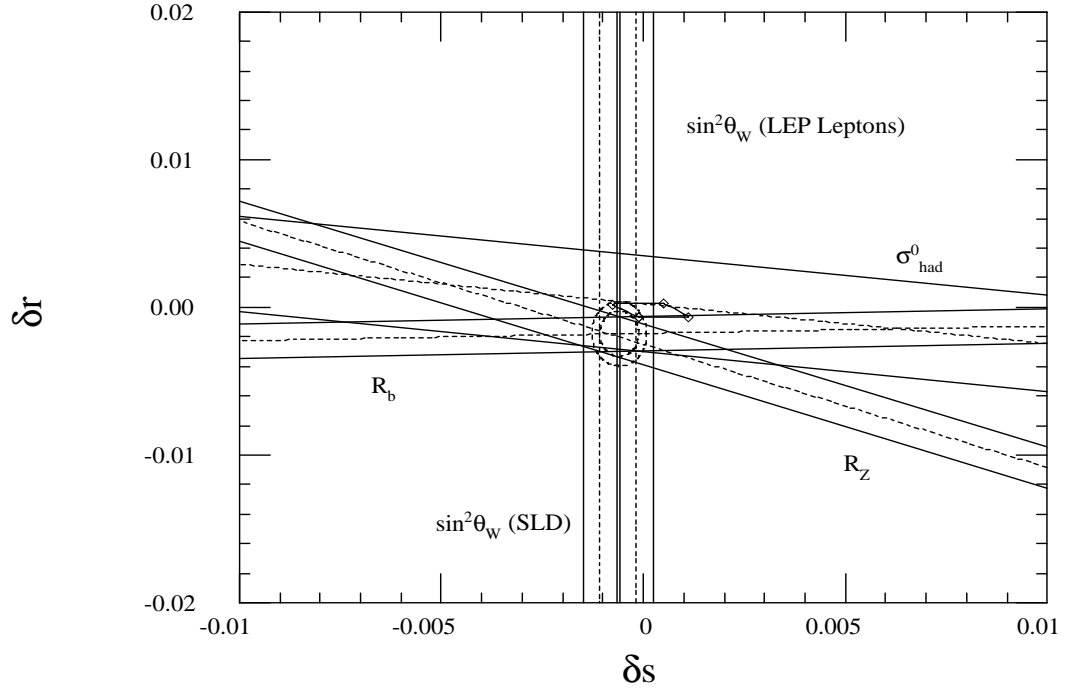


Fig. 16. Plots of simultaneous fits to $\sin^2 \theta_W^{eff}$ and Zb vertex parameters, projected into the δr (R_b -like) and $\sin^2 \theta_W^{eff}$ plane.

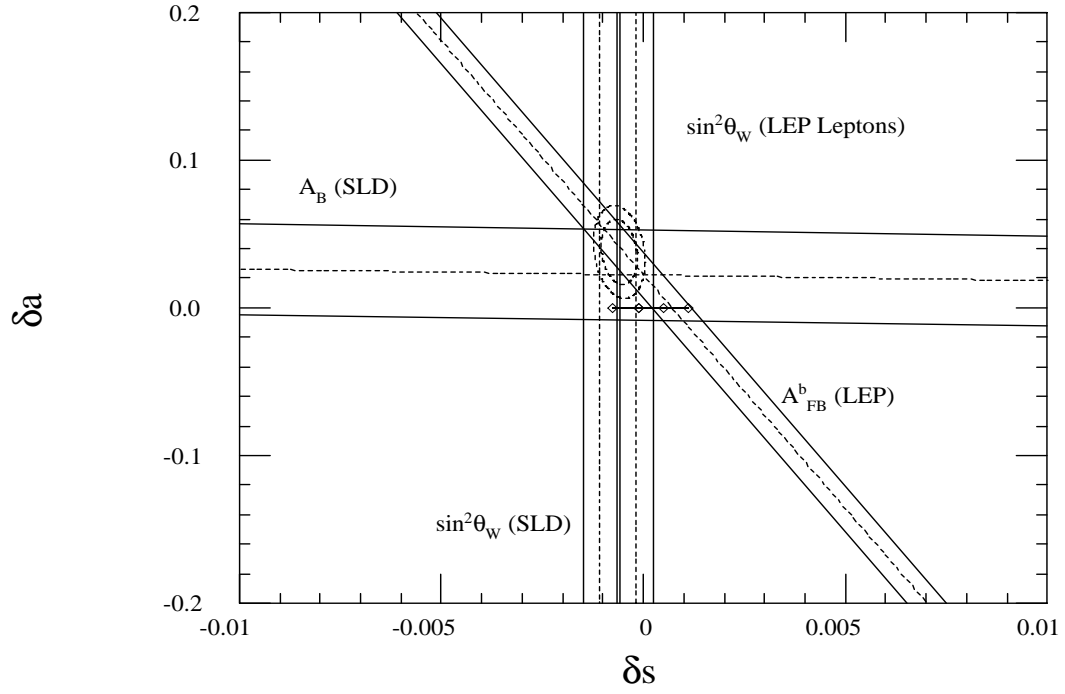


Fig. 17. Plots of simultaneous fits to $\sin^2 \theta_W^{eff}$ and Zb vertex parameters, projected into the δa (A_b -like) and $\sin^2 \theta_W^{eff}$ plane.

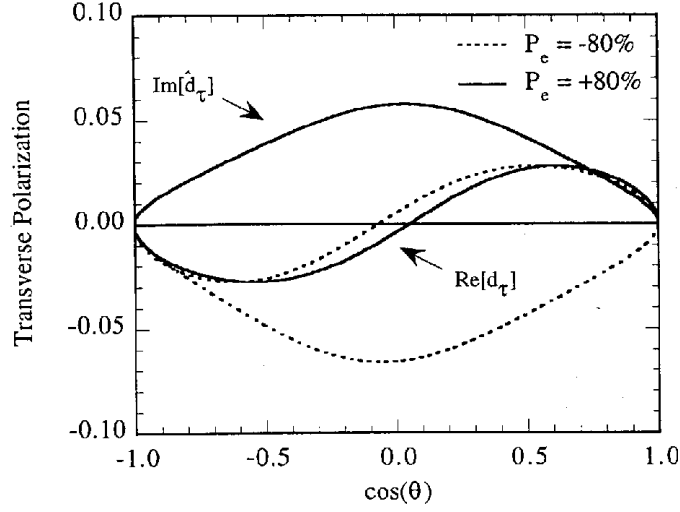


Fig. 18. Plot of the $\cos \theta$ dependence of the tau transverse polarization generated by anomalous weak magnetic (d_τ) and weak electric (\tilde{d}_τ) dipole moments.

11 Tau Lepton Anomalous Moments

The inclusion of an ad-hoc term

$$\mathcal{L}_{anom} = \frac{i}{2} \bar{\tau} [\sigma^{\mu\nu} q_\nu (d_\tau - i\tilde{d}_\tau \gamma^5)] \tau Z_\mu \quad (34)$$

in the $Z - \tau$ coupling gives rise to complex anomalous weak magnetic (d_τ) and weak electric (\tilde{d}_τ) dipole moments, which can be constrained with SLD data. These terms generate net transverse polarization of the taus from Z^0 decay (see Fig. 18), which can be detected by fitting the quadruple-differential cross section

$$\frac{d^4 \sigma_{L,R}}{dx^* d\Omega^* d \cos \theta} \quad (35)$$

separately for left- and right-handed electron beams.⁹ Here, x^* and Ω^* are the scaled energy and solid angle of the charged track in the cms frame of one-prong tau decays; the one-prong decay modes used in the analysis are $\tau \rightarrow \pi \nu_\tau$, $\tau \rightarrow \rho \nu_\tau$, $\tau \rightarrow e \bar{\nu}_e \nu_\tau$, and $\tau \rightarrow \mu \bar{\nu}_\mu \nu_\tau$. The results of these fits for the SLD data are shown in Table 5.

Table 5. Comparison between SLD and pre-existing limits on the weak electric and weak magnetic moments of the tau lepton.

Parameter	SLD Limit ($\times 10^{-17}$ e cm)	Pre-existing Limit ($\times 10^{-17}$ e cm)
$ Re(d_\tau) $	< 8.5	< 8.1
$ Im(d_\tau) $	< 6.3	< 8.1
$ Re(\tilde{d}_\tau) $	< 9.1	< 0.32
$ Im(\tilde{d}_\tau) $	< 6.6	< 1.0

12 Summary and Outlook

The polarization and vertexing capabilities of the SLC/SLD are an ideal combination for the exploration of electroweak physics at the Z^0 pole. SLD has made major contributions to the body of electroweak results in a number of arenas, including the single best measurement of the weak mixing angle, and unique measurements of the coupling of heavy flavors to the Z^0 . The SLD is currently at the beginning of a long run with a projection of 500,000 recorded Z^0 decays. With this sample at hand, the SLD expects an uncertainty on the weak mixing angle of $\delta \sin^2 \theta_W^{eff} = \pm 0.00020$, leading to a 4σ discrepancy with LEP if the central values remain unchanged. In addition, the SLD expects to achieve or exceed the current LEP accuracy for most heavy quark coupling measurements, with a largely independent approach. In the lepton sector, the SLD should arrive at a dominant $e - \mu$ universality constraint from its mu-pair angular distributions, and improve its limits on anomalous tau couplings, which are already the best in the world in the case of the weak magnetic moment.

References

- [1] K. Baird *et al.* (SLD Collaboration), in these proceedings.
- [2] K. Abe *et al.*, SLAC-PUB-7385, Nucl. Instrum. Methods A **400**, 287 (1997).
- [3] LEP Electroweak Working Group, “A Combination of Preliminary Electroweak Measurements and Constraints on the Standard Model,” in preparation.
- [4] K. Abe *et al.* (SLD Collaboration), Phys. Rev. Lett. **78**, 2075 (1997).
- [5] M. Peskin and T. Takeuchi, Phys. Rev. D **46**, 381 (1992).
- [6] K. Abe *et al.* (SLD Collaboration), Phys. Rev. Lett. **80**, 660 (1998).
- [7] J. Stav and H. Olsen, Phys. Rev. D **52**, 1359 (1995).
- [8] T. Takeuchi, A. Grant, and J. Rosner, FERMILAB-CONF-94-279-T, August 1994.
- [9] E. Torrence, SLAC-R-0509, June 1997 (Ph.D. Thesis).